Technichal University of Munich
Max Planck Institute for Extraterrestrial Physics
High-Energy Astrophysics

Bachelor's Thesis in Physics

Gamma-Ray Search from SN2014J Radioactivity

Suche nach Gamma-Strahlung aus der Radioaktivität der SN2014J

Sandra Resch

August 10, 2018

Supervisor: Prof. Dr. Roland Diehl

Contents

1 Introduction

Nuclear fusion processes started at the beginning of the universe with the big bang. During the first few minutes of the universe mainly hydrogen, helium and a small abundance of lithium were the only elements created through nucleosynthesis. With the expansion of the universe these processes stopped and consequently those elements were the basis of the continuing evolution and are the most abundant elements in the universe. However, the earth consists of a huge variety of elements and isotopes besides hydrogen and helium. [4] There must be mechanisms in the universe which produce heavier elements and spread it all over the cosmos. For the fusion of nuclei there has to be enough energy to overcome their repulsive Coulomb force. This condition can be reached in a dense accumulation of stellar matter held together by its own gravity. Nucleosynthesis occurs during the evolution of stars and especially their end of evolution when their supply of fusion material is exhausted. If the mass of the star is higher than eight solar masses ($M_\odot$), it can end up in an enormous explosion called supernova. During these events enough energy is released through fusion processes that also very massive elements can be produced. There are different types of supernovae depending on the mass of the exploding star. Low and medium mass stars ($0.4-8\ M_\odot$) end up as white dwarfs which can accumulate mass if they have a companion star in a binary system and, reaching a certain mass limit, finally end up in a thermonuclear explosion. These type Ia supernovae are of special interest as they can be used to measure distances in the universe as so called standard candles. Their explosions and the resulting spectra show similar behaviour and yet neither their progenitors nor the explicit explosion mechanisms are distinctly identified. Models and simulations are created for a better understanding and to develop and improve them they have to be compared to real observations. [13]
Supernovae can be traced by their emission of gamma-rays with spectrometers outside the earth' atmosphere like the International Gamma Ray Astrophysics Laboratory INTEGRAL. The spectrometer aboard INTEGRAL (SPI) consists mainly of 19 cooled germanium detectors partially shadowed by a coded mask. It is able to detect gamma-rays with a high energy resolution in a range of 20 keV to 8 MeV. The recorded spectra can be analysed and information about the origin of the detected gamma-rays can be determined. As the spectra almost entirely consist of background photons, a data model is used to distinguish between celestial contribution from the source and mainly instrumental background. One origin of celestial gamma-rays is the radioactive decay. If a point source like a supernova is in the spectrometers field of view, the gamma-ray lines of radioactive material produced and ejected during the explosion can be analysed. Information about the amount of ejected mass, their kinematics and the light curve shape of the

supernova can be extracted and compared to predictions of models. [9]
The aim in this thesis is to have a closer look at the spectra of gamma-ray lines resulting from radioactive decays of the material produced and ejected by the type Ia supernova SN2014J. Chapter 1 is giving an overview over stellar evolution and especially type Ia supernovae, their progenitor systems, explosion mechanisms and nucleosynthesis. After explaining the production mechanism of gamma-rays and the detection method with the SPI detector on INTEGRAL in chapter 3, the analysis process of the detected data is described in detail in chapter 4. Chapter 5 presents the application of these methods and further analysis of the gamma-ray lines of three different radioactive elements ^{56}Co, ^{48}V and ^{57}Co.

2 Type Ia supernovae

2.1 Stellar evolution and explosions

After reaching the main sequence, the temperature (T) in the inner core of a star has reached a value that thermonuclear reactions set in and lead to a hydrostatic equilibrium. The radiation pressure ($\propto T^4$) prevents the star from a gravitational collapse. [24] The first longest lasting nuclear reaction is the burning of hydrogen in a proton-proton chain reaction. If the temperature is higher than $\simeq$ 10 MK, the kinetic energy of two protons is high enough that they can overcome their Coulomb barrier and form a deuterium core by emitting a β^+. With the fusion of the deuterium and another hydrogen core ^{3}He is produced which again can fuse to the stable nucleus ^{4}He and two protons in the reaction $2\ {}^3He \longrightarrow\ {}^4He + 2p$. With this process hydrogen can be converted to helium at temperatures ranging from $10 - 14$ MK. For even higher temperatures there is another hydrogen burning process which includes heavier elements, the so called carbon-nitrogen-oxygen-cycle. The result is basically the same as in the p-p-process, but the cycle starts with the proton capture of an isotope of carbon (^{12}C) which originates from the explosion of stars of previous generations. It is called a cycle because the end product of the reaction is again ^{12}C and an α, hence the CNO isotopes only act as a catalyst. The CNO-cycle needs higher temperatures and the occurence of carbon to start and is therefore dominant in more massive stars ($>$ 1.3 $M_\odot$). During the evolution of a main sequence star, the pp-chain is the main energy source. [7] [12] If the hydrogen reserves are exhausted and the central hydrogen burning phase (main sequence phase) ends, the final stage of the stellar evolution begins. The stars have helium rich cores and an envelope consisting of hydrogen. Hydrogen is still converted to helium in a thin layer around the core. As there are no fusion processes in the core, the radiation pressure decreases. Thus, the core shrinks due to its gravitational

pressure, which increases its temperature. If the temperature in the core is higher than $\simeq$ 100 MK, the burning of helium starts. Via the triple-α process it is converted into ^{12}C and subsequently into ^{16}O. If the helium is exhausted in the core, a thin He burning shell remains. The resulting CO core begins to contract and gains mass due to He burning in the helium shell. After He burning, the evolution of the star depends on the mass of the CO core and accordingly the initial mass of the star.

If the star is heavier than 10 $M_\odot$, it undergoes more burning stages up to the production of iron group nuclei. After carbon burning ends, the neon burning starts releasing mainly ^{24}Mg through the fusion with helium. After oxygen burning the final silicon burning stage is ignited which produces nuclei with higher atomic numbers through successive α-processes up to the unstable intermediate ^{56}Ni. The radioactive nickel decays via the β^+ decay to ^{56}Co and finally into the stable ^{56}Fe. As iron (^{58}Fe) has the highest binding energy per nucleon, the fusion up to heavier nuclei is endothermal and would not release any energy. Therefore after developing an iron core the iterative shell burning ends. Because of the escaping neutrinos, which are created especially with increasing temperatures and densities, carrying away energy the last burning stages scale with higher powers of the temperature and proceed faster. With the end of fusion processes the only force countervailing the gravity is the electron degeneracy pressure due to the Pauli exclusion principle. The Fe rich core collapses under its own gravity until it reaches critical densities. The strong nuclear force gets repulsive and the created shockwave accelerates the material outwards. This process is called a core collapse supernova where 99% of the energy is carried away by neutrinos. The remnant is either a neutron star or a stellar black whole. [7], [13]

In contrast to those heavyweights, very low mass stars (< 0.4 $M_\odot$) stay over 50 Gyr on the main sequence so the final stage of the evolution could not yet be observed.

If the mass of a star lies between the two limits corresponding to a mass of the CO core lower than 1.1 $M_\odot$, the ignition temperature for carbon burning can not be reached and the electron degeneracy pressure prevents the star from collapsing under its own weight. The overlying shells are loosing mass through stellar winds and thermal pulses. The latter are caused by alternating helium and hydrogen burning in the shells. The ejected material is called a planetary nebula surrounding the remaining electron degenerate CO core which is also known as a white dwarf (WD). WD's have a size of $\sim 10^3$ km and masses of ~ 1 $M_\odot$ with core densities of $\sim 10^6$g cm^{-3}. Without any energy source the white dwarf will cool down. [7] [13]

However, the white dwarf can interact with a companion star in a binary system. Through mass transfer or merging it can reach a critical mass, the

so called Chandrasekhar-limit which is about 1.46 $M_\odot$. If the mass of the WD exceeds this limit, the gravitational force overcomes the electron degeneracy pressure and the WD explodes as a thermonuclear type Ia supernova (SNIa). The classification of supernovae is based on their spectra. As type Ia supernovae originate from CO white dwarfs having rejected most of their envelope, they lack hydrogen and helium lines but show silicon lines because of the thermonuclear burning of carbon and oxygen during the explosion. Other type I supernovae don't show silicon lines and type II supernovae have hydrogen lines in their spectra. [13] The following subsections describe the evolution up to an explosive state and the exact explosion mechanism of a type Ia supernova.

2.2 Progenitor models

There is more than one possible scenario for a white dwarf to reach an explosive state and it is very likely that various progenitor and explosion models contribute to the observed variety of type Ia supernovae. Models with working explosion mechanisms are compared to characteristics like for example the right amount of produced elements and their ejection velocities as well as the light curve shape and luminosity. In the following the three most likely progenitor scenarios which agree best with the observed SNIa rates are presented. [14]

2.2.1 Single-degenerate model

The initial situation of the single-degenerate model is the electron degenerate white dwarf in a binary system with a non degenerate companion star. That could be either a main sequence or a giant-like star. The material of the companion is bound by gravity within a region shaped like a teardrop called Roche-lobe illustrated in figure 2.1. If the star is overfilling its Roche-lobe, matter is transferred to the WD through the peak of the Roche-lobe, the inner Lagrangian point, where the gravity of the two stars cancels out. As a result the white dwarf is continuously accumulating mass in the form of hydrogen or helium which starts to burn and increases the inner density of the WD due to the release of gravitational energy. When the white dwarf is reaching the critical Chandrasekhar mass, and therefore a critical density, the carbon starts to burn. That can lead to a thermonuclear explosion. [21]

2.2.2 Double-degenerate violent mergers

In the double-degenerate model, the two binaries are electron degenerate and massive (> 0.9 $M_\odot$) white dwarfs. If the white dwarfs are less massive and

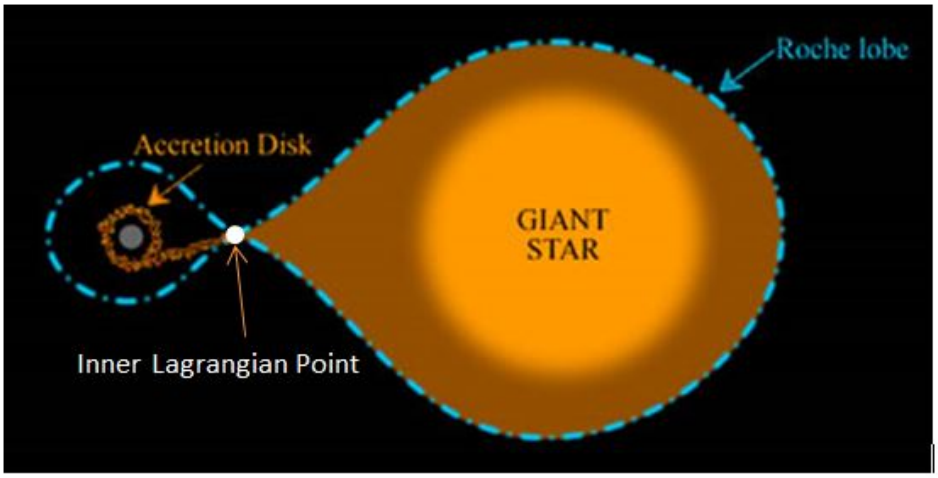

Figure 2.1: Roche-lobe of two stars in a binary system with mass transfer through the inner Lagrangian point. From: [25]

the mass ratio is not close to unity, the merger only causes the disruption of one white dwarf. Accretion of that material by the second star leads to a transformation into a oxygen-neon-magnesium white dwarf which ends in a collapse leaving behind a neutron star when reaching the critical mass. [22] The figure 2.2 shows a binary system of two white dwarfs with masses of 1.1 $M_\odot$ and 0.9 $M_\odot$ orbiting each other as the more massive companion deforms the other by tidal interaction, transfers mass onto it and they finally merge. At this point the temperature and the density are high enough to ignite carbon burning and finally trigger an explosion. [14]

2.2.3 Sub-Chandrasekhar-mass scenario

In contrast to the other scenarios this model assumes that a thermonuclear supernova can also be triggered without a WD reaching the critical mass. In this scenario a CO white dwarf is in a binary system with a helium-rich companion and is accreting a helium shell. If that layer of helium is reaching a critical density it ignites explosive helium burning. The shockwave can compress the WD which possibly leads to an explosion although the WD does not need to reach the critical Chandrasekhar mass. Therefore, the model is also called double-detonation scenario. [37] [14]

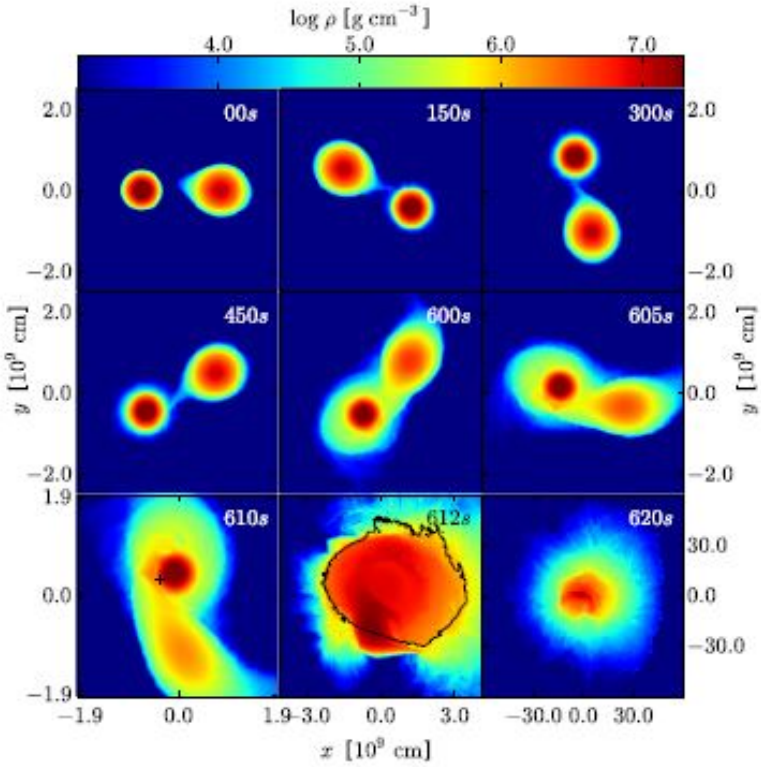

Figure 2.2: Last few orbits of two white dwarfs in a binary system which are merging and triggering a detonation (black cross at 610 s). From: [14]

2.3 Explosions and nucleosynthesis

After having discussed how white dwarfs may reach an explosive state, in the following the most important aspects of a thermonuclear supernova are discussed: the explosion mechanism and the thermonuclear burning during the explosion.

2.3.1 Turbulent deflagration model

Once the burning is ignited a combustion wave starts to propagate through the white dwarf leaving behind elements with higher binding energies, also called nuclear 'ashes'. This burning can propagate through heat conduction at a subsonic velocity in the deflagration mode, enabling the star to expand during explosion. Furthermore, the combustion can be driven by a supersonic shock wave in a detonation. Those combustion modes are affecting the stratification and amount of produced elements, as the nucleosynthetic production of elements is depending on the temperature and therefore on

the density of the matter. At lower densities, primarily in the outer regions of the exploding white dwarf, mainly intermediate mass elements of the Si-group are produced because the energy for further fusion is not sufficient. If the density is very high ($\sim 10^7$ g cm^{-3}), the system is in a nuclear statistical equilibrium and only the relative binding energies are important. Figure 2.3 shows the relation between the density structure of the white dwarf and the created nucleosynthetic products during burning. If burning takes place in a detonation mode in a Chandrasekhar mass white dwarf, the high velocity of the burning front leaves no time for the star to expand and thus the fuel burns at the high initial density of the white dwarf in nuclear statistical equilibrium shifting nucleosynthesis towards iron group elements. As it can be seen in figure 2.3 almost only iron group elements are produced (solid green line). That is in conflict with some type Ia supernovae observations, which show less iron group but more intermediate mass elements. [14] [27] The second idea could be that burning takes place only in deflagration mode

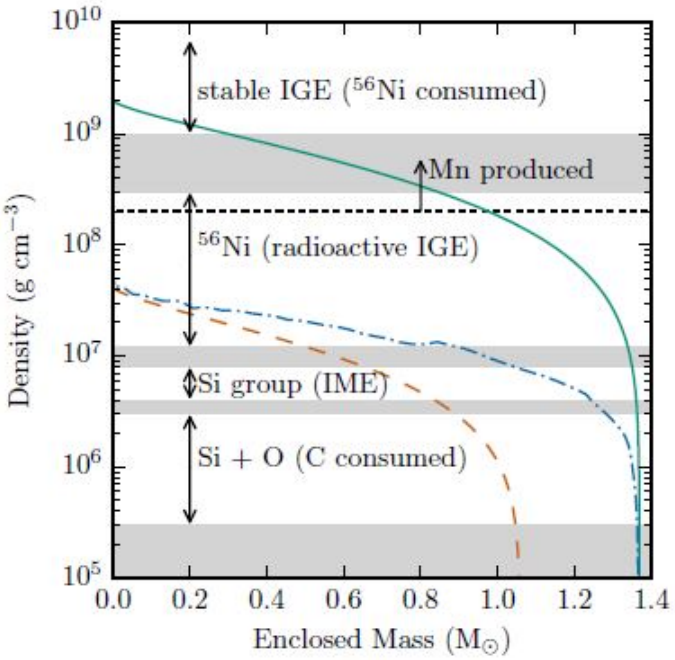

Figure 2.3: Relation between density structure of a white dwarf and the nucleosynthetic products in different burning modes: detonation (solid green) and delayed detonation (dot-dashed blue) of a near-Chandrasekhar WD and detonation of a $1.05M_\odot$ WD (dashed orange). From: [27]

which is the assumption of the turbulent deflagration model. In contrast to a laminar deflagration which would propagate too slowly and thus not re-

lease enough energy for a type Ia supernova, turbulences and instabilities are taken into account which accelerate the flame. The down to small scales eddied flame has a significantly enlarged surface area which is increasing the propagation velocity and thus the energy release. Figure 2.4 shows a three-dimensional model of a propagating deflagration starting in multiple ignition spots around the center and the described flame surface. The turbulent deflagration model can only reproduce dimmer type Ia supernovae but not the whole variety of observed events. For that the kinetic energy and the ^{56}Ni production are too low. Also the ejecta composition does not match with observations because it is too inhomogeneous and chemically mixed. [26]

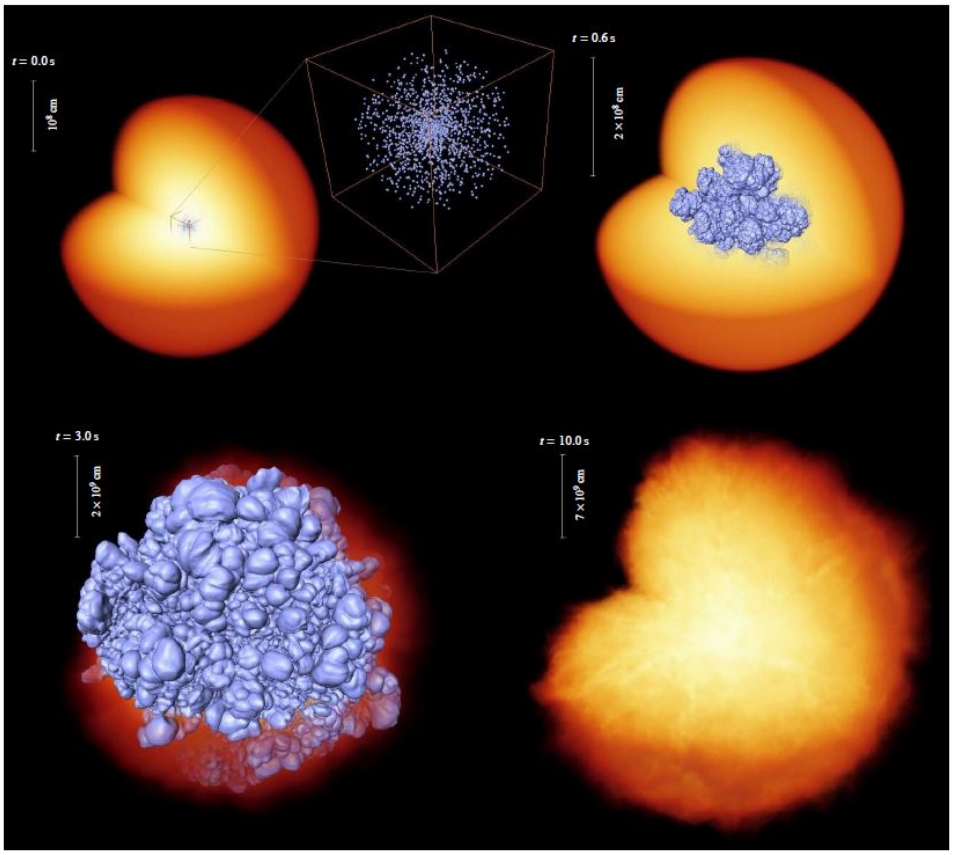

Figure 2.4: Turbulent deflagration model simulation with logarithmic density (yellow to red), eddied flame surface (blue) and multiple ignition spots. From: [26]

2.3.2 Delayed detonation model

In order to improve shortcomings of the described explosion model, a third model is proposed in which a detonation follows the turbulent deflagration and therefore this model is called delayed detonation scenario. The explosion again starts with a subsonic turbulent deflagration that is expanding the fuel and building up eddies through instabilities. The greatest uncertainty of this model is, how the deflagration transforms to detonation mode. It seems plausible that it is triggered as the flame structure significantly changes in later burning stages at densities around 10^7 g cm^{-3} and high turbulent velocity fluctuations. [26] If this is assumed as a parameter such a transition in the delayed detonation scenario can be simulated as it is shown in figure 2.5 where the detonation is triggered in the first snapshot. The next two figures demonstrate that the deflagration keeps the white dwarf expanding while the detonation front passes. [26] The speed of the propagating deflagration thus determines the density of the fuel in the moment of detonation and this affects the energy release and ^{56}Ni production. The strength of the deflagration varies depending on the ignition method. If there are only few ignition spots, the deflagration propagates slow and the detonation can burn a lot of fresh and dense fuel. [14] Figure 2.3 shows that this leads to a strong production of iron group elements. The density of the fuel in the center of the white dwarf is higher than in the outer layers, so the outcome is dominated by a iron-group rich core surrounded by intermediate mass elements, which is in good agreement with observations. The density structure of a delayed detonation of a Chandrasekhar mass white dwarf is plotted in blue in figure 2.3. Through variation of the ignition it is possible to reproduce brighter and also dimmer SNe, if the deflagration dominates. However, the exact transition from deflagration to detonation, especially in the microscopic view, remains unclear. [26]

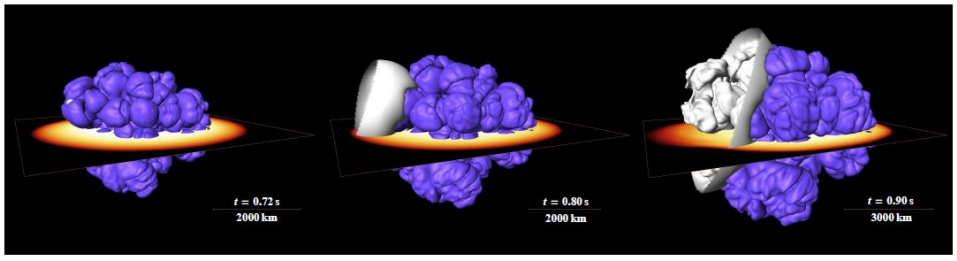

Figure 2.5: Turbulent deflagration flame (blue surface) with a delayed ignition of a detonation wave (white surface) propagating through the star. The logarithm of the density is shown in the intersecting plane. From: [26]

2.3.3 Double-detonation model

As already mentioned when introducing the progenitor model, it is also possible that a white dwarf never reaching the critical Chandrasekhar mass can lead to a type Ia supernova. The white dwarf has accumulated a layer of helium or hydrogen burning to helium. If this layer is thick and massive enough, the compression of the material can lead to sufficient heating, triggering a detonation. The shock wave propagating into the core of the CO white dwarf leads to a second detonation disintegrating the star in a thermonuclear supernova explosion. The burning of the rather thick helium shell contributes to the produced element yields. Especially the amount of elements produced through α-capture, like ^{36}Ar,^{40}Ca, ^{44}Ti, ^{48}Cr or ^{52}Fe is increased. Nevertheless predictions for the ^{56}Ni yield and thus the brightness of this explosion mechanism agree with observations. In figure 2.3 the density profile of the detonation of a 1.05 $M_\odot$ white dwarf is shown in orange which produces less iron group elements as the delayed detonation scenario does. [26] [14] [27]

2.3.4 Model criteria

In order to develop explosion models they have to be compared with observations. One important diagnostic is the amount of produced ^{56}Ni. The reason for that is connected with the so called lightcurve which describes the evolution of brightness in time past explosion. The absolute luminosity and the bolometric lightcurves are very distinctively for type Ia supernovae. As a consequence they can be used as so called 'standard candles' to measure distances in the universe and the cosmological expansion rate. If the absolute luminosity is known and the apparent brightness is measured, the distance to the observed object can be calculated. As a normalization the Phillips relation is used. It relates the shape of the lightcurve and the absolute luminosity and says that the fainter a supernova is, the faster it declines from its maximum. The lightcurve has a maximum peak at around 30 days after explosion in the optical radiation range. The expansion of the explosion material leads to an increasing permeability for the photons. The gamma-rays produced by nuclear processes like the decay of ^{56}Ni interact and exchange energy with the exploding matter through the photoelectric effect, Compton scattering and pair production. [15] Thus, the amount of produced ^{56}Ni is directly linked to the energy input into the material. The system gets thermalized and is able to absorb and emit radiation over all wavelengths which means that it is a black body. Thus, the supernova emits black body radiation which has a spectral distribution following Planck's law

and depending only on the temperature. [5] The optical lightcurve results from the emission with a black body temperature in the optical light. As the remnant cools down, the brightness decreases rapidly. The long term evolution of the lightcurve is powered by the radioactive decay of the ^{56}Ni with a lifetime of 8.8 days and the decay product ^{56}Co having a longer lifetime (111.3 days). [20] In the gamma-ray regime the lightcurve is different. It reaches its maximum after around 70-90 days past explosion when the envelope becomes transparent for gamma-rays coming from the radioactive decay of the ^{56}Co and only a minor fraction is scattered. Typical ^{56}Ni yields are in the range of 0.3 to 0.9 $M_\odot$ but there are also subluminous supernovae with only $\sim$ 0.1 $M_\odot$ and superluminous supernovae with a higher observed nickel mass. Other requirements for explosion models are that the production of ejecta is in agreement with observations, especially a sufficient amount of intermediate mass elements is produced in the outer layers, and that the kinematics, which can be examined through Doppler broadening, match with observations. How such spectra and lightcurves can be observed and analysed will be discussed in the following chapters. [8] [14] [13] [7]

3 Gamma-rays and detection with SPI

3.1 Gamma-rays from radioactive decays

A way to detect elements produced in supernovae is via gamma-ray measurements. Production channels for high energy photons are through matter-antimatter annihilation, particle acceleration or deceleration and the radioactive decay, which is the focus of this chapter. Radioactive decay happens when an unstable isotope decays into a stable state by releasing energy. The released energy is emitted in photons and the kinetic energy of particles. There are several subtypes of decays. The α-decay, where a heavy parent atomic nucleus emits a ^{4}He nucleus and also releases binding energy in form of kinetic energy of the decay products. The β-decay can be divided into three types: in a β^--decay, a neutron in the atomic nucleus is converted into a proton, releasing an electron and an electron antineutrino. The inverse case is the β^+-decay where a proton is converted into a neutron emitting a positron and an electron neutrino. Energy is released again in form of kinetic energy of the lepton and the neutrino. If an electron of an atom has a high probability density near the nucleus it can be captured by the nucleus, converting also a proton into a neutron under the emission of an electron neutrino, resulting in the process ${}^A_Z X_N + e^- \rightarrow {}^A_{Z-1} X_{N+1} + \nu_e$. This process competes with the β^+-decay but as the electron capture process needs less energy than the creation of the positron, in some cases only electron

capture is possible. Often those decays do not end in a stable ground state but in an excited state of the nucleus. Through electromagnetic interaction the nucleus de-excites into a lower state under the emission of a photon with the energy difference between those two levels. This process can occur multiple times until the ground state is occupied leading to a cascade-like de-excitation. As an example figure 3.1 shows the radioactive decay scheme of ^{56}Ni. With a half-life time of $T_{1/2} = 6.10$d nickel transforms through electron capture into an excited state of ^{56}Co. The gamma transitions of the levels are given together with their energy and the number of transitions per 100 decays in brackets. The lifetime of such an excited stage is $\sim 10^{-9}$ s, so the γ-decay is a very fast process and does not noticeably contribute to the total half-life time. The ^{56}Co itself also is unstable but has a longer half-life time ($T_{1/2} = 77.12$d). [7]

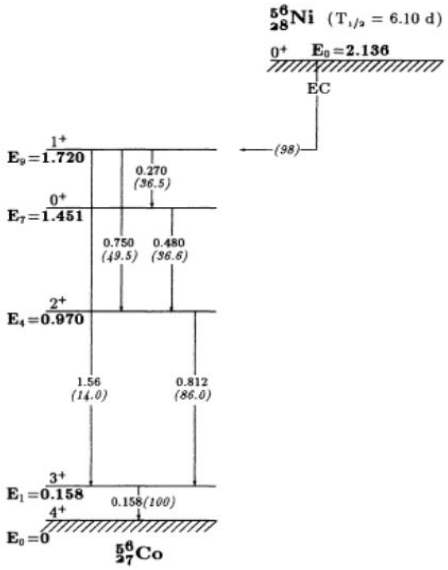

Figure 3.1: Simplified decay scheme of ^{56}Ni. From: [20]

3.2 The SPI detector on INTEGRAL

Gamma-rays have to be detected outside the earth's atmosphere which is shielding high energetic radiation. Therefore, a satellite, the Gamma Ray Astrophysics Laboratory (INTEGRAL), was launched into space by ESA in 2002. The initially planned three-year-mission has been extended every two years since then due to its scientific success. INTEGRAL is orbiting earth in a highly elliptical orbit with a period of three days at a perigee of 7000 km and an apogee of 150000 km, to avoid unwanted background from the ra-

diation belts near earth. Aboard the spacecraft there are four instruments, the two monitor instruments JEM-X and OMC for observations in the x-ray and optical energy range and the two main instruments, the SPI detector and the IBIS imager. The left picture of figure 3.2 shows an overview over the spacecraft. On the right-hand side the Spectrometer on INTEGRAL (SPI) and its components are shown, which are explained in more detail in the following. [9] [8] The main instrument of SPI is its camera consist-

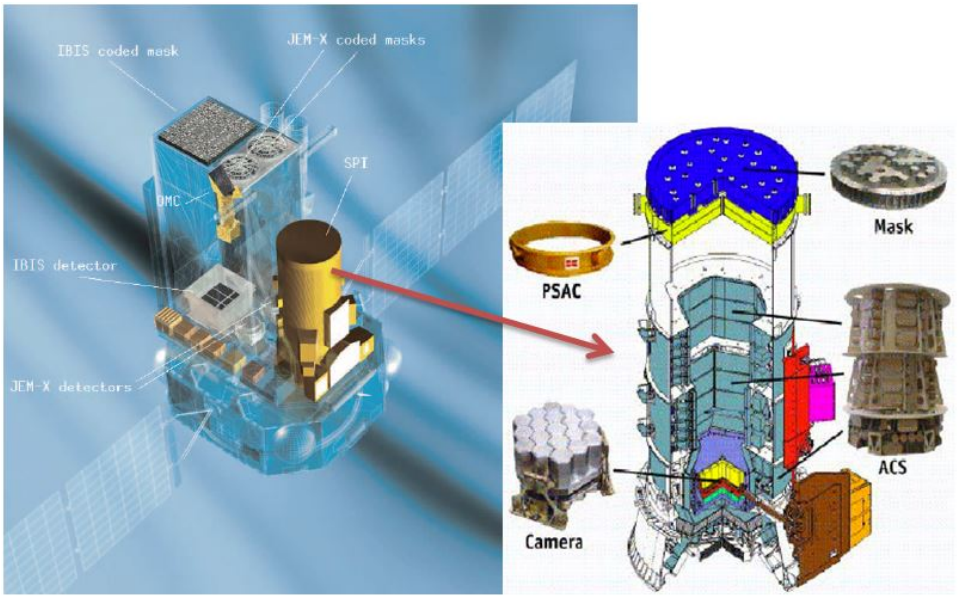

Figure 3.2: Left: Impression of the INTEGRAL spacecraft with the four instruments. Right: Schematic picture of the SPI spectrometer and its main components. From: [36] and [9]

ing of 19 separated germanium semiconductor detectors. Semiconductors can be described by the general energy band structure of crystalline materials which can be divided into three groups: insulators, semiconductors and conductors. The difference between them is the size of the band gap. The schematic representation in figure 3.3 shows the principle band structure. The lowest band is the valence band containing the electrons of the outer atomic energy shells. The conduction band contains free electrons able to traverse the entire crystal allowing electric conduction in the material. The space between those two bands is the energy gap not containing any energy levels. The width of this forbidden area determines the characteristics of the material: a large gap negates the possibility of thermal excitation of the electrons, making the material an insulator. In contrast, in a metal there is no energy gap at all and the valence and conduction band overlap. Electrons can consequently move freely in the conduction band and the application of an electric field leads to a current. In the middle frame of figure 3.3 a

semiconductor is shown where the energy gap is intermediate in size. If there is enough thermal energy, few electrons from the valence band can be excited that they can cross the gap into the conduction band leaving behind a hole at its original location. Applying an electric field causes both the electrons in the conduction band as well as the holes in the valence band to move. Having a net positive charge, the holes act like positive charge carriers under the influence of an electric field. The concentration of the created electron-hole-pairs depends on the thermal energy and therefore on the temperature. At room temperature ($T = 300$ K) one out of 10^9 atoms in germanium is ionized. [18] In order to use the germanium as a detector, it has to be cooled to minimize charge excitation due to thermal effects and thereby decreasing thermal noise in the electronics. Electron-hole-pairs are created by the interaction of incoming gamma-rays with the material via photo-electric absorption, Compton-scattering or pair production transferring energy to the electrons and the Ge material. An electric field is applied, making the electrons drift to the one side and the holes to the other side of the detector. The electrical charges are collected at the electrodes at the boundaries of the semiconducting material on a capacitor where they can be measured as pulses. To minimize the collection time, the applied voltage should be sufficiently high so that the charge carriers drift at high velocities. To increase the contribution of electrons to the current, the semiconductor can be doped with donor impurities which have one more valence electron. That can easily be excited to the conduction band and can also fill up holes. Advantages of using germanium as detector material are the high atomic number (Z=32) which corresponds to a high photoelectric absorption probability and the high energy resolution due to a small bandgap. [18] [17]

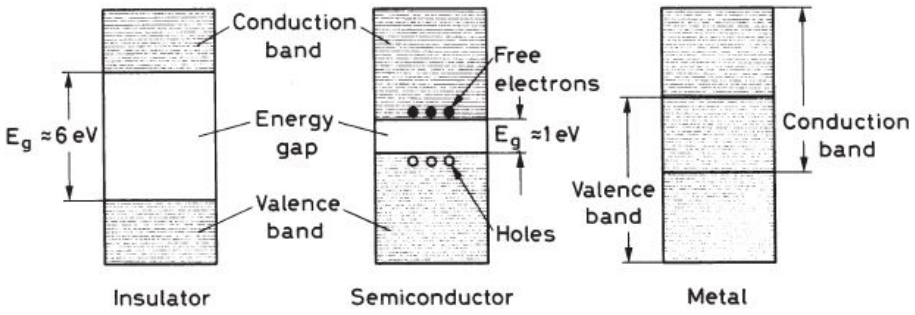

Figure 3.3: Band structure of the different material types. From: [18]

On SPI there are 19 high-purity n-type germanium detectors densely packed in a hexagonal arrangement with a detection area of 250 cm^2. The hexagonal shape of the detectors was chosen with regard to optimal use of space. On the left-hand side of figure 3.4 a photo of the detector arrangement is shown. To identify the particular detectors they are numbered in an order illustrated

in figure 3.5 starting with the lowest number in the middle. They are fixed on a Be plane and cooled down to temperatures between $85 - 90$ K with a cryogenic system. The applied voltage between the electrodes to collect the produced electron-hole pairs was 4 kV in the beginning of the mission and now is 2.5 kV. As the detectors can be damaged by radiation which decreases the energy resolution, they are regularly annealed which means that they are heated up to 105 °C for one or two days and the crystal structure is restored. Undamaged detectors have an energy resolution of 3 keV at $1300 - 1800$ keV and events in an energy range of 18 keV $-$ 8 MeV can be detected.

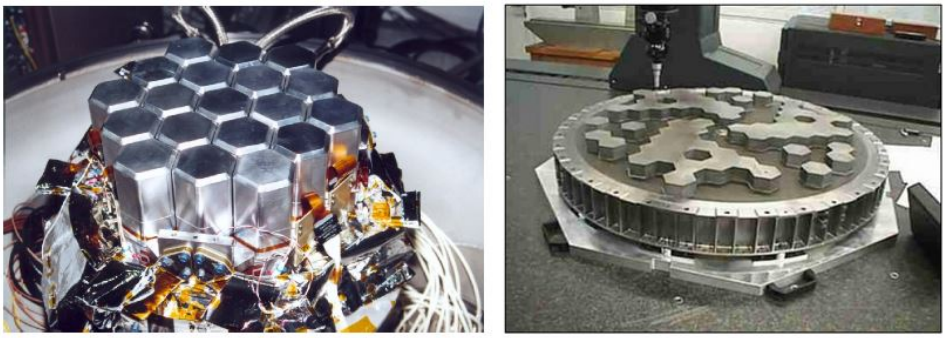

Figure 3.4: Left: SPI camera with 19 germanium detectors. Right: Coded mask with tungsten blocks. From: [35]

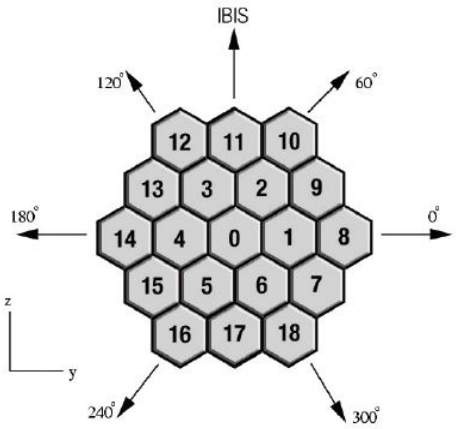

Figure 3.5: Arrangement and numbering of the 19 detectors. From: [9]

The second important component of the spectrometer is the coded mask which is installed 1.71 m above the detector plane and weighs about 140 kg. The right picture of figure 3.4 shows a photo of the mask. It consists of 63 opaque and 64 translucent hexagonal pixels of which the opaque ones are made of 30 mm thick tungsten. The mask is blocking parts of the field of

view and as a result some parts of the camera are shadowed. Depending on the relative position of a detector to the direction of SPI, the mask casts a specific shadowgram on the detector. Thereby the gamma-ray point source can be localized. The field of view of the spectrometer is 16° and its angular resolution is 2.5°.

The last two components which are shown in figure 3.2, are two anticoincidence systems. The ACS (active anticoincidence system) enclosing the instrument, is made of BGO crystals with the main function of reducing background events. If it interacts for example with a charged particle or gamma-rays from outside the field of view, a veto signal is triggered for 725 ns. Particles which do not reach the ACS are rejected by the plastic scintillator anticoincidence subassembly (PSAC). It reduces especially the background coming from prompt interactions with the mask. After separate observation intervals of $\sim$ 2000 s, the SPI telescope is reoriented so that it surrounds the target direction in a 5×5 grid with steps of 2.1 degrees altering the shadowgram of the source in the detector. That process, which helps to gain additional modulation of the imaging information, is called dithering. [35] [8]

4 Data and analysis

4.1 SPI primary data

The events, that are detected by the germanium detectors, are received by the front-end electronics which measure the event time with an accuracy of 102.4 ns. The data space consisits of the detector and the signal pulse height. It also rejects events when receiving a veto signal, counts the events and supervises the detector dead-time, which is the time needed for the pulse to return to zero-level and therefore separate two events in the detector. [17] At the INTEGRAL's Science Data Centre (ISDC) an energy calibration is done to convert pulse height units to channel space and convert that in turn into keV-space. In the low energy range (20-2000 keV), six strong lines between 100 and 1800 keV of all orbits are used for the calibration. Furthermore, count histograms per detector and per spacecraft pointing are created. Figure 4.1 shows an example of those processed event data for one detector (no. 0) and one pointing. [9]

Those data sets together with information about detector dead times, start and end times and also the direction coordinates are provided for further analysis. In the data $\sim$ 99% of the counts originate from the underlying instrumental background. Therefore the background counts cannot simply be subtracted from the data, but our analysis method compares predictions

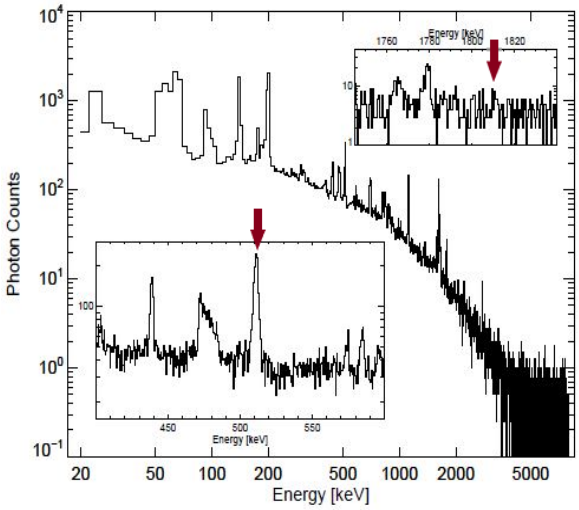

Figure 4.1: Data histogram for detector no. 0 and one pointing. The two smaller pictures inserted show the energy range where the brightest positron-electron annihilation line at 511 keV and the 1809 keV ^{26}Al line are shown. From: [9]

from models with the data structure and fits for the parameters θ_n. It is described by the following equation:

$$d_{i,j,k} = \sum_{l} R_{l;ijk} \sum_{n=1}^{N_s} \theta_n S_{nl} + \sum_{n=N_s+1}^{N_s+N_b} \theta_n B_{n;ijk} \tag{1}$$

The event count per pointing i, detector j and energy bin k $d_{i,j,k}$ is written as a sum of sky model components S_n and background components $B_{n;ijk}$. The sky model components with N_s parameters θ_n describe the data from e.g. the point source as photon source intensity per sky direction l which is linked to the data via the instrument response matrix $R_{l;ijk}$. [9] The background and the celestial lines are discussed in more detail in the chapters 4.3 and 4.4.

4.2 Statistical methods

As described in formula 1, the model is fitted to the data. A model can be a simple class of functions, like a straight line or Gaussians, but it can also originate from an underlying theory. These models can be modified by a number of parameters with the aim of finding the set which provides the best agreement between model and data. This agreement is measured by a so called figure-of-merit-function. Therefore, the best-fit-parameters are those leading to a minimum in that function. Nevertheless, real, measured

data never exactly fits the model. As measuring data is a statistical process it is prone to measurement errors. To complete the fitting procedure after finding the best-fit parameters, the goodness-of-fit should be checked.

The fitting algorithm that is used utilizes the maximum likelihood method. Assuming a set of N data points (x_i, y_i) should be fitted to a model with M parameters a_j related through a function

$$y(x) = y(x; a_1...a_M) \tag{2}$$

the aim is to find parameters so that the model and the data are in good agreement. In other words: the likelihood to obtain the data, plus or minus measurement errors on each data point, given a specific model described by a set of parameters, should be maximized. The general principle is therefore called the maximum likelihood estimation. To describe the process a Gaussian probability distribution is used whereas the counts detected by SPI are Poisson distributed which will be explained later. Instead of maximizing the probability which is the product of the probabilities of each point

$$P \propto \prod_{i=1}^{N} \left\{ exp\left[-\frac{1}{2} \left(\frac{y_i - y(x_i)}{\sigma} \right)^2 \right] \Delta y \right\} \tag{3}$$

for a Gaussian probability distribution, the negative of its logarithm neglecting constants

$$\sum_{i=1}^{N} [y_i - y(x_i; a_1...a_M)]^2 \tag{4}$$

can be minimized over $a_1...a_M$ which leads to the same result and is also known as least-squares fit. If the standard deviation σ of each data point (x_i, y_i) is taken into account, the equation to minimize to get the best-fit parameters changes into:

$$\chi^2 = \sum_{i=1}^{N} \left(\frac{y_i - y(x_i; a_1...a_M)}{\sigma_i} \right)^2 \tag{5}$$

To get a first estimate of the goodness of fit, the reduced χ^2_{red} which is defined as

$$\chi^2_{red} = \frac{\chi^2}{\nu} \tag{6}$$

should approximately be equal to one. In the equation above $\nu = N - M$ are the degrees of freedom.

Furthermore, it has to be tested whether the fit is statistically significant or not. This can be done by a chi-square-test. If the minimum chi-square for a specific data and parameter set is found, modifying the parameter set leads to an increase of the chi-square. The difference in χ^2 defines a confidence

region, which means a region in the M dimensional data space containing a certain percentage of the total probability distribution. If the difference in degrees of freedom $\Delta dof = 1$, the square root of chi-square $\sqrt{\Delta\chi^2}$ gives the confidence level in units of the standard deviation σ. A probability of 1σ means that the confidence region encloses the true values of the parameters 68.3 % of the time repeating the measurements an infinite number of times. A 2σ confidence region corresponds to 95.4 % and a 3σ interval corresponds to 99.73 %. In order to find out the significance e.g. of a signal it can be compared to the null hypothesis, which gives the probability that the data is measured by chance. Then the null hypothesis can or can not be excluded to a certain level of significance that is required. [23]

The distribution of a number of independent and rare events occurring in a specific interval of time or space, like the event counts detected by the SPI detector, can be expressed through a discrete probability function, the Poisson distribution:

$$f(n, \lambda) = e^{-\lambda}\frac{\lambda^n}{n!} \tag{7}$$

The expected number of events per interval is described by λ whereas the actual observed number of events is n. The positive number λ is also equal to both the mean and the variance of the Poisson distribution. For an increasing number of λ, the distribution turns into a Gaussian distribution as it is shown in figure 4.2. [11]

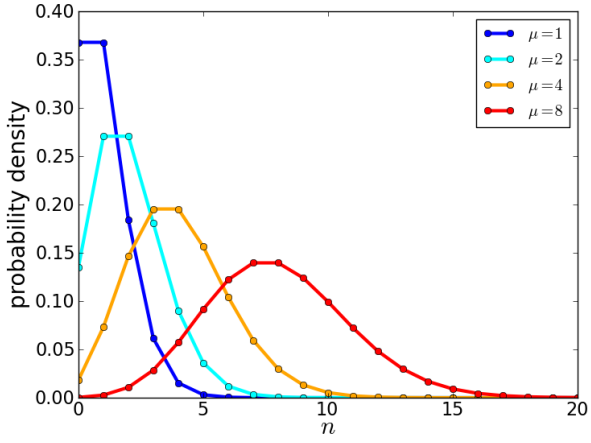

Figure 4.2: Poisson distributed probability density functions for different numbers of λ. From: [2]

Another criterion if the data fits the model good are the residuals. Residuals are defined as the difference between the real, observed data points and the model fitted points. They should be distributed normally around the mean

$\mu = 0$ with a standard deviation of $\sigma = 1$. If the model does not fit well, there are outliers with larger residuals. They are determined by the following equation:

$$R = \frac{D - B}{\sqrt{B}} \tag{8}$$

The modeled background counts B, which are composed of continuum and lines, are subtracted from the event counts which means the data itself. The residuals are normalized to the statistical fluctuations of the background which follow Poisson statistics and thus are calculated as $\sqrt{B}$. [6]

4.3 Instrumental background

4.3.1 Background origins

The dominating background originates mainly from the interaction of energetic particles with the spacecraft. These originate from solar activity which varies in an eleven-year cycle and also from solar flares which cause impulsive ejections of charged particles. Another source are the Van-Allen radiation belts which irradiate the spacecraft at perigee passage but also afterwards. When the instrument passes the region of radiation belts, measurements are stopped. The interaction of particles with atoms and nuclei of the material of the spacecraft can lead to nuclear transitions which release prompt photons. There are also delayed background photons which can originate from nuclear interactions of cosmic ray photons creating secondary particles, excited nuclei and radioactivity affecting the measurements even when the spacecraft has already passed this region. Bremsstrahlung is caused by secondary particle interaction where they partially loose their energy. If those photons are not blocked by the ACS, they are detected and show in the spectrum. The bremsstrahlung dominates the continuum of the spectrum, the photons with specific energies that come from nuclear de-excitations and therefore from radioactive decay or resonance absorption show up as well-defined, narrow lines. The background description is not based on a theoretical model but on empirical data because many underlying processes are of unknown origins. [9]

4.3.2 Background model

The background is composed of specific lines and an underlying continuum. The used model for each line is a Gaussian function with an amplitude A_0, the energy position of the centre E_0 and the width σ:

$$G(E; E_0, \sigma) = A_0 exp\left(-\frac{(E - E_0)^2}{2\sigma^2}\right) \tag{9}$$

The Gaussian is convolved with a one-sided exponential T(E) which accounts for decreased charge collection efficiency due to detector degradation with time between the annealings:

$$T(E;\tau) = \frac{1}{\tau} exp\left(\frac{E}{\tau}\right) \tag{10}$$

with the degradation parameter τ. To model the continuum a power law function is used,

$$C(E;\alpha,c_0) = \left(\frac{E}{E_m}\right)^{\alpha} \tag{11}$$

where c_0 is a constant scaling factor and E_m is the centre energy in the region of interest. In figure 4.3 the model of a spectrum near the strong ^{26}Al line is shown where all the assumed identified energy lines caused by isotopes are modeled as individual components above the smooth continuum. The

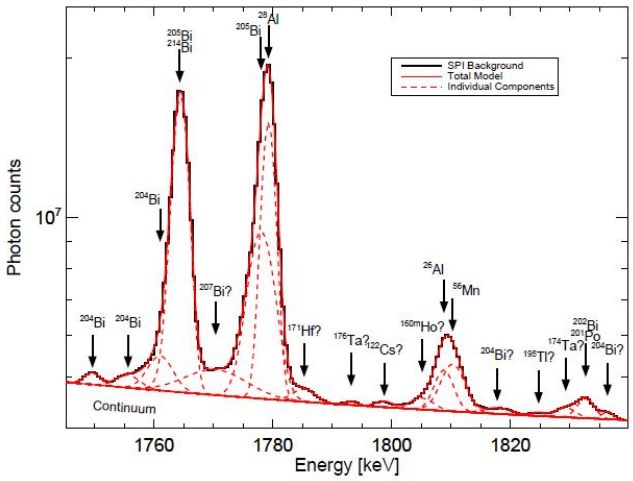

Figure 4.3: Background spectrum with model decomposed into various lines and continuum. From: [9]

whole energy range is divided into parts with a range of about 100 MeV and the background model is fitted for each detector and orbit separately. The results are stored in a database. The goodness-of-fit is controlled through its χ^2 value and a consistency check is done by the comparison of the spectral parameters to the ones of neighbouring lines and other detectors. [9]

4.4 Celestial gamma-ray lines

Detector ratio patterns which show the relative intensities among the 19 detectors are created for each energy bin k with a width of 0.5 keV below the instrumental resolution separately for lines and continuum to get the

sky model components B_{jk}. Through a maximum likelihood fit using Poissonian statistics the intensity scaling factors θ for the background and sky model components can be determined. To distinguish between celestial and background components of the model it is in first order assumed that the instrumental background remains constant over long periods ($\sim$ 1 revolution) and spectral shape and relative detector ratios do not vary, whereas secondly the celestial signal of the camera varies during dithering and create different shadowgrams which are shown in figure 4.4. During a dithering process the telescope is reorientated and with every re-orientation the intensity distribution among the detectors varies where white symbolises full exposure and black means that it is completely shadowed. [9]

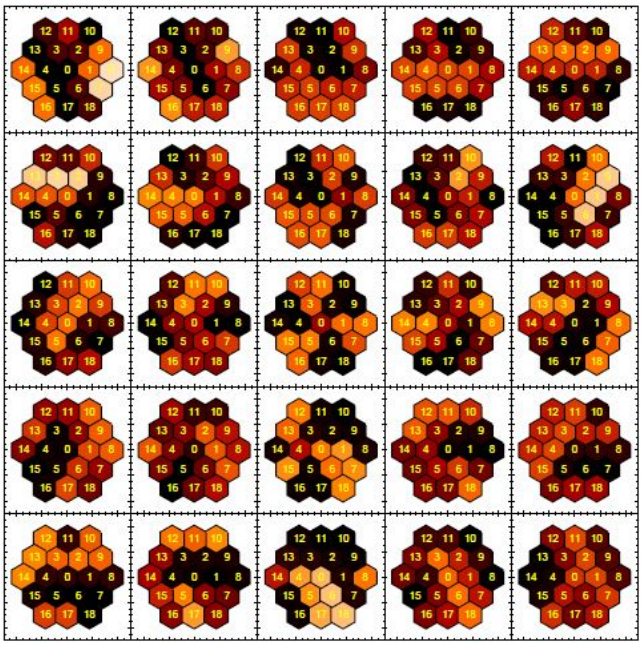

Figure 4.4: Colour coded shadowgrams on the Ge camera during the dithering process. From: [9]

The calculations are done by a program called SPI-modfit which gives spectra of the sky of the chosen energy range, source location and revolutions as flux per energy bin as a result.

To analyse the spectra, we assume a model that can be fitted to lines originating from radioactivity gamma-rays from celestial sources like a type Ia supernova. The model consists of lines that are assumed to have Gaussian shapes and maybe still an underlying continuum. According to this a

Gaussian function with an added constant is used as a model:

$$f(A_0, E_0, \sigma, c) = A_0 exp\left(-\frac{(E-E_0)^2}{2\sigma^2}\right) + c \tag{12}$$

The amplitude A_0, the centroid energy E_0, the width σ and the offset c are the parameters of the model. The fit is done with a Monte-Carlo Markov-Chain which searches for the minimum of the χ^2. Therefore some start parameter values have to be chosen and the numeric method approximates with little random steps and some previously set iterations the smallest value of χ^2 and gives back the values of the best fit parameters and their errors. The parameter E_0 contains information about the kinematics of the gamma-ray source. The bulk of radioactive atoms emitting the photons with the specific energy may not be at rest but move towards or away from the SPI detector. This results in a Doppler shift of the wavelength and thus the energy of the gamma-ray. If the source of the wave is moving towards the spectrometer, the wavelength is slightly shifted to energies higher than those moving away from the detector. The formula for that shift can be written as

$$\Delta E = E \cdot \frac{v_{bulk}}{c} \tag{13}$$

E is the rest frame energy of the photon, v_{bulk} its velocity relative to the observer, c the speed of light and ΔE the resulting Doppler shift. [33] Another information about kinematics of the supernova explosion is contained in the width of the gamma-ray line. Naturally lines from atomic transitions are not sharp but have a narrow natural line width due to the uncertainty principle of quantum mechanics which leads to an uncertainty in energy because of a finite lifetime. Additional broadening is caused by the instrumental resolution σ_{instr} of the SPI detector which varies with energy. A third broadening process is due to the velocity spread of the atoms in the gas caused by thermal motions which is called thermal broadening or Doppler broadening. The velocity spread can be calculated by the following equation:

$$v_{spread} = \frac{\sigma_{Doppler}}{E_0} \cdot c \tag{14}$$

where E_0 is the fitted line energy (already Doppler shifted), $\sigma_{Doppler}$ is the Doppler broadened line width and c the speed of light. [19] The broadening of the line with respect to the instrumental resolution σ_{instr} at a certain energy can be written as

$$\sigma = \sqrt{\sigma^2_{Doppler} + \sigma^2_{instr}} \tag{15}$$

5 Results

The gamma-ray source that is chosen to be analysed in that chapter is a type Ia supernova, SN2014J, which was the closest type Ia supernova observed in the past few decades. It was discovered in the nearby star-forming galaxy Messier 82 at a distance of $\simeq 3.3$ Mpc. The explosion date was set to 14 January with an uncertainty of 0.21 d and 16.3 days later, on 31 January, the observation with INTEGRAL was conducted until 26 June, day 164 past explosion, with a total exposure of 7 Ms. It was terminated by visibility constraints. Therefore the revolution numbers 1380 to 1428 have been chosen for the analysis, with a gap between 23 April and 27 May. One sky model component ($N_S = 1$) is used to model the data and the background is modeled per revolution. In the following, gamma-ray spectra from three different elements ejected by the SN2014J are analysed. [34] [10]

5.1 ^{56}Co

The first isotope is ^{56}Co which is expected to be produced in high amounts during the explosion of a CO white dwarf and powers the light curve as mentioned in Chapter 2. We do not search for ^{56}Ni because the lifetime of ^{56}Ni ($\tau \sim 8$ d) is too short to observe gamma-rays at MeV energies as the supernova envelope is expected to be still too opaque to γ-rays. Thus, we look for the radioactive decay of ^{56}Co into the stable ^{56}Fe with a half-life of $T_{1/2} = 77.27$ d. It decays via electron capture and β^+ decay and emits a lot of photons with a multitude of different energies. With a branching ratio of 100% a gamma-ray with an energy at rest of 846.771 keV is emitted and with a branching ratio of 67.6% a 1238.282 keV photon is produced. As the analysis of the ^{56}Co lines has already been done by Diehl et al. [10] here only the 846.771 keV line analysis is reproduced to confirm our analysis method. [31] To search for this line an energy range from $780 - 920$ keV is chosen to cover effects from Doppler shift and broadening. Figure 5.1 shows the spectrum over the whole observation time of ~ 147 d. The Gaussian line model presented in chapter 4.4 is fitted per 0.5 keV bins. The resulting spectrum is binned to energy bins of 10 keV and the fit is shown in red. It has an amplitude of $A = 5.44 \pm 1.95 \cdot 10^{-6}$ ph cm^{-2}s^{-1}keV^{-1}, a width of $\sigma = 17.07 \pm 0.76$ keV and an offset of $c = 5.65 \pm 9.32 \cdot 10^{-7}$ ph cm^{-2}s^{-1}keV^{-1}. The centroid energy of $E_0 = 844.73 \pm 6.42$ keV is slightly shifted to the red. The error bars result from Poissonian statistical uncertainties of the event counts which are propagating through the maximum likelihood fitting of the data model. The null hypothesis that there is only an underlying continuum, can be excluded with a statistical significance of 3.32 σ. The intensity of the ^{56}Co gamma-rays should vary in time so the spectrum is split into 4 different epochs to do time resolved analysis. From the day of explosion the

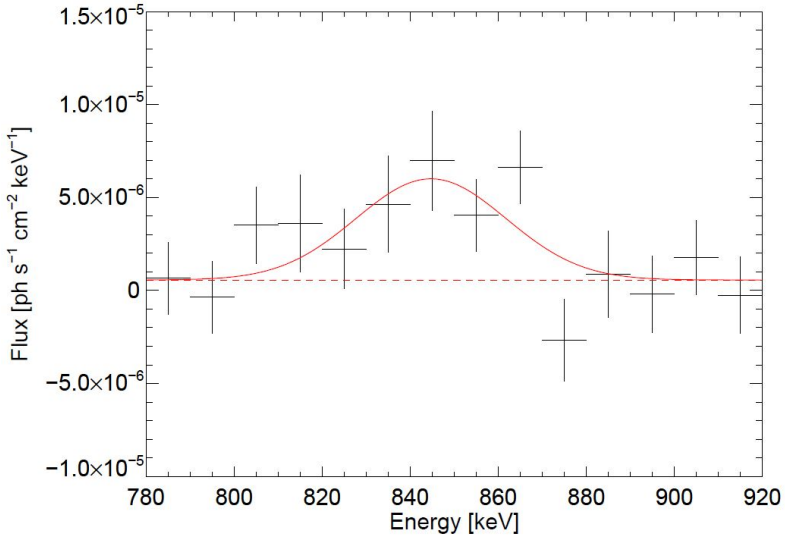

Figure 5.1: Spectrum near the 846.771 keV line with a fitted Gaussian function (red) and fluxes rebinned to 10 keV energy bins

optical depth decreases over time which results in a rising emission of gamma rays. This phase is covered by the first three epochs with the post-explosion days 16.3-41.3 (epoch 1), 41.3-66.3 (epoch 2) and 66.3-99.1 (epoch 3). The fourth epoch (134.8-164.0 post-explosion days) shows the phase of a rather transparent supernova. The spectra of the four different epochs are shown in figure 5.2. Gaussian functions with an underlying continuum are fitted to the respective spectra. This time in addition to the broad ^{56}Co line, a second narrow Gaussian line is fitted which can not be assigned clearly to ^{56}Co or ^{56}Ni decay. The flux of those main broad peaks which are associated with the ^{56}Co gamma-ray line are calculated. Therefore the flux per energy has to be integrated over energy which is equivalent to the area under the Gaussian curve and can be calculated by the formula:

$$F = \sqrt{2\pi} \cdot A_0 \cdot \sigma \tag{16}$$

with A_0 representing the amplitude and σ representing the width of the Gaussian. [3] The calculated flux, the center and the width of the fit are listed in table 5.1. The values of the fluxes for the first two epochs are consistent with the values of Diehl et al. [10] within the calculated uncertainties. Overall the calculated fluxes are lower than the ones in the paper. The resulting light curve is shown in figure 5.3 where it can be clearly seen that especially the flux of the third epoch is too low as it is expected to be the point of the highest intensity. The horizontal error bars represent the chosen epochs. The mass of emitted ^{56}Ni can be estimated through the line fluxes of the decay product ^{56}Co. That calculation makes use of the fact

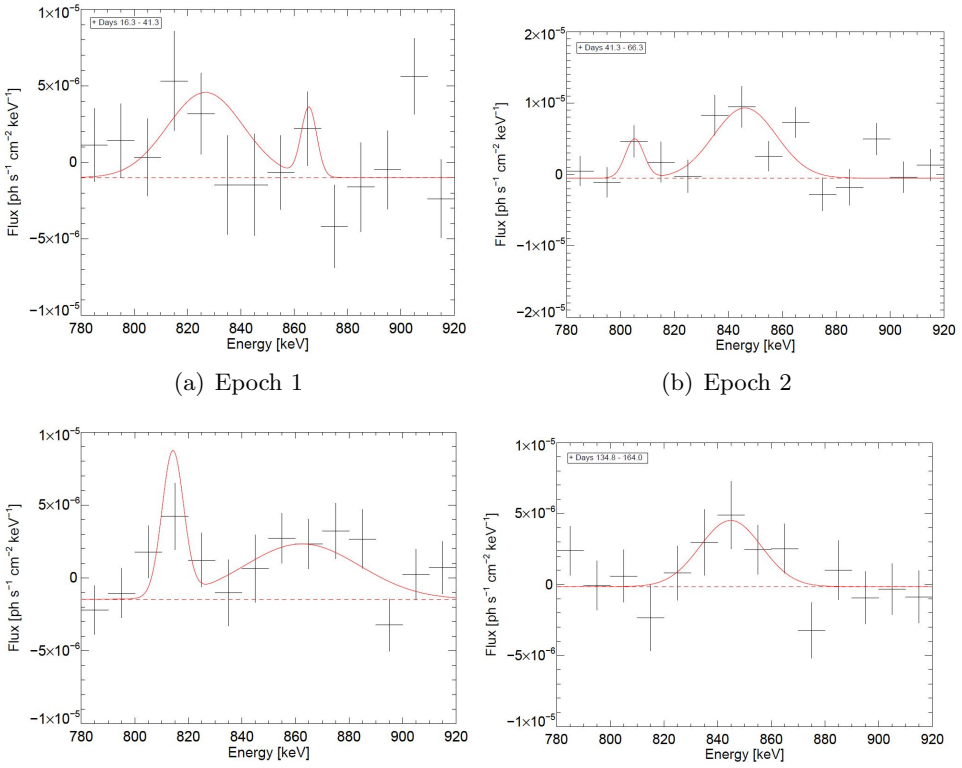

(a) Epoch 1 (b) Epoch 2

(c) Epoch 3 (d) Epoch 4

Figure 5.2: Spectrum with 10 keV bins and Gaussian fits in red near the 846.771 keV line of ^{56}Co in the four different epochs

Time	Flux [10^{-4}ph cm^{-2}s^{-1}]	Center [keV]	Width [keV]
Epoch 1	1.98 ± 0.59	826.7 ± 0.9	14.2 ± 1.0
Epoch 2	2.64 ± 0.66	846.2 ± 4.3	11.7 ± 1.0
Epoch 3	2.06 ± 1.00	862.5 ± 1.2	21.6 ± 1.1
Epoch 4	1.34 ± 0.49	844.9 ± 5.0	11.5 ± 0.7

Table 5.1: Parameters of the 847 keV line fit

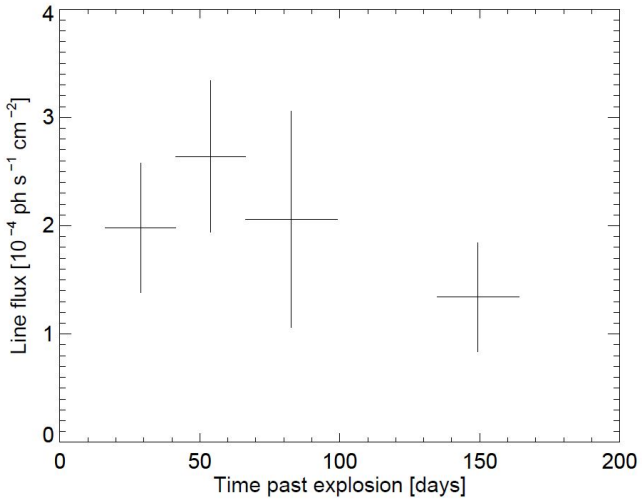

Figure 5.3: Flux variations in time past explosion from the 847 keV line of ^{56}Co

that every photon that is detected by the SPI camera in the 847 keV line originates from ^{56}Co atoms of the supernova explosion. Determining the number of gamma-rays being detected in that time and thus the number of ^{56}Co atoms, the total mass can be calculated. The flux of a γ-ray decay line from a radioactive point source can be described by the following formula:

$$F = \frac{b \cdot A}{4\pi r^2} \tag{17}$$

with the branching ratio b, the distance r between source and detector and the activity A of the radioactive element:

$$A = -\frac{dN(t)}{dt} = \lambda \cdot N_0 \cdot e^{-\lambda t} \tag{18}$$

N_0 is the initial number of parent nuclei, N(t) is the number of parent nuclei remaining after the time t and λ is the decay constant defined as $\lambda = {}^{ln(2)}/_{T_{1/2}}$. [1]
With the equations 17 and 18 a formula for the mass calculation can be derived and expressed by

$$M = \frac{F \cdot m_{atom} \cdot 4\pi r^2}{b \cdot \lambda \cdot e^{-\lambda t}} \tag{19}$$

where m_{atom} is the atomic mass of the observed element and t is the mean value of the time after explosion in epoch x. The radius r is the distance between the supernova and the spacecraft INTEGRAL which is $r \simeq 1.02 \cdot 10^{20}$ km. As an approximation it is assumed that the spread of the gamma-rays is spherically symmetric. The mass values calculated separately for

every epoch are averaged and the resulting mean is $M = (0.24 \pm 0.08)M_{\odot}$. This value also differs from the ^{56}Ni mass of (0.49 ± 0.09) $M_{\odot}$ derived in [10].

5.2 ^{48}V

The photons from the decay chain of the next radioactive isotope, ^{48}Cr, are searched for in the spectrum. Through the radioactive decay of $^{48}\text{Cr} \longrightarrow {}^{48}\text{V}$ with a half-life of $T_{1/2} = 21.56$ h, vanadium is produced. The vanadium itself decays via electron capture and β^+-decay into the stable ^{48}Ti with a half-life of $T_{1/2} = 15.974$ d. The radioactive decay chain of ^{48}Cr is chosen for the research because models predict promising yields of ^{48}Cr in the order of $\sim 10^{-4}M_{\odot}$ from delayed detonation models and even $\sim 10^{-2}M_{\odot}$ in helium detonation models and the half-life of the decay product ^{48}V could be sufficient to measure gamma-rays of it. [28] [29] With intensities of 99.98% and 97.5% gamma-rays with the energies 983.517 keV and 1312.096 keV are emitted and thus energy bands of $910 - 1050$ keV and $1240 - 1380$ keV were chosen for analysis. [30]
In order to review the goodness-of-fit of the data model in those two energy bands and to make sure that there are no extreme outliers, the residuals are plotted in histograms shown in figure 5.4. A Gaussian function is fitted to that histogram which is illustrated in blue. The residuals should follow a normal distribution with the mean $\mu = 0$ and the standard deviation $\sigma = 1$ if the model fits the data which should normally be the case as the data almost entirely consists of background events. [6] In fact, the model fits well and the parameters of the Gauss fit are: $\mu = -0.002 \pm 0.009$ and $\sigma = 1.006 \pm 0.009$ for energy range $910 - 1050$ keV and $\mu = 0.032 \pm 0.001$ and $\sigma = 1.012 \pm 0.009$ for the energy range $1240 - 1380$ keV. As there is no excess in positive values, consequently no signal is expected.
Due to the short lifetime of ^{48}V, the spectrum again is split into time intervals which are fitted separately for the analysis of the spectrum of the SN2014J in those energy ranges. Three epochs are chosen: 16.3-30 d, 30-50 d and 50-70 d past explosion.
The fit failed to get any signal with a sufficient statistical significance so only upper limits can be determined. A source can have a given probability of not being detected up to a certain intrinsic intensity. The largest value of that intensity is called an upper limit. The threshold for the probability here are 99.73 percent which equals 3σ. The upper limit value is determined as follows: First the model described in equation 12 is fitted but the only variables varied are the amplitude and the offset. The parameters σ and E_0 of the fit are fixed. As the velocity values from ^{56}Co are already determined by Diehl et al., these values are used to calculate the Doppler shift and broadening for lines of other isotopes. The assumption is made that

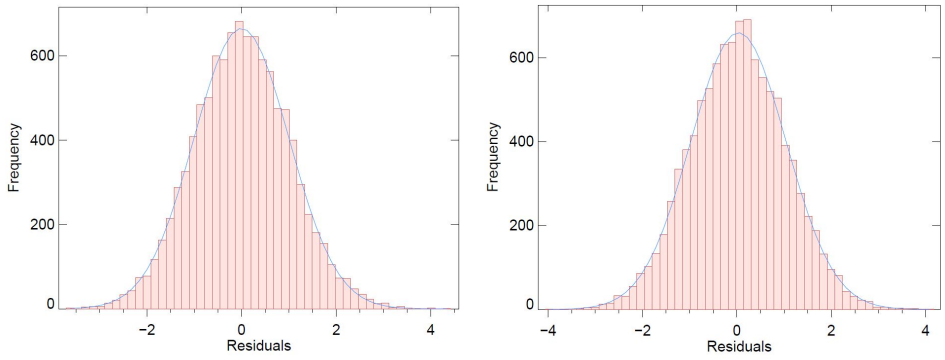

(a) Energy range 910 − 1050 keV (b) Energy range 1240 − 1380 keV

Figure 5.4: Histogram plots of the normalized residuals for the two different energy ranges

Time [d]	Flux [10^{-4}ph cm^{-2}s^{-1}]	Center [keV]	Width [keV]
16.3 - 30.0	2.36	961.8	16.2
30.0 - 50.0	2.09	961.8	16.2
50.0 - 70.0	1.60	989.3	13.0

Table 5.2: Parameters and upper limit fluxes of the ^{48}V line near 984 keV in three different epochs

the propagation speed and velocity spread is approximately the same for all ejected elements. The values for the different time epochs are stated in table 7.1 in the appendix. Using equations 13 and 14, the expected width and the centroid energy of the model can be calculated. The fit gives a minimum χ^2_{min} with the best fit parameters A_0 and c which is illustrated as a blue point where the blue lines intersect in figure 5.5. Finally the upper limit value of A is determined with the following procedure. χ^2 is calculated for different values of A in steps of $0.1 \cdot 10^{-6}$ which results in the parabola shown in figure 5.5. The values of A at which $\chi^2 - \chi^2_{min} = 9$ are searched for which equals a statistical significance of 3σ with $\Delta dof = 1$. The two resulting intersections are marked with red points where the related lower value of A is the lower limit and the higher value is the upper limit. [16]
For the three epochs of the energy range from $910 - 1050$ keV the Gaussian line fits (blue) with the parameters A_0 and c and the calculated upper limits for the fluxes of the lines (red) are shown in the figure 5.6. The flux is again binned into 10 keV energy bins for a better representation which makes up the horizontal error bars. The values of the fixed parameter σ and E_0 and the upper limit flux are listed in table 5.2.

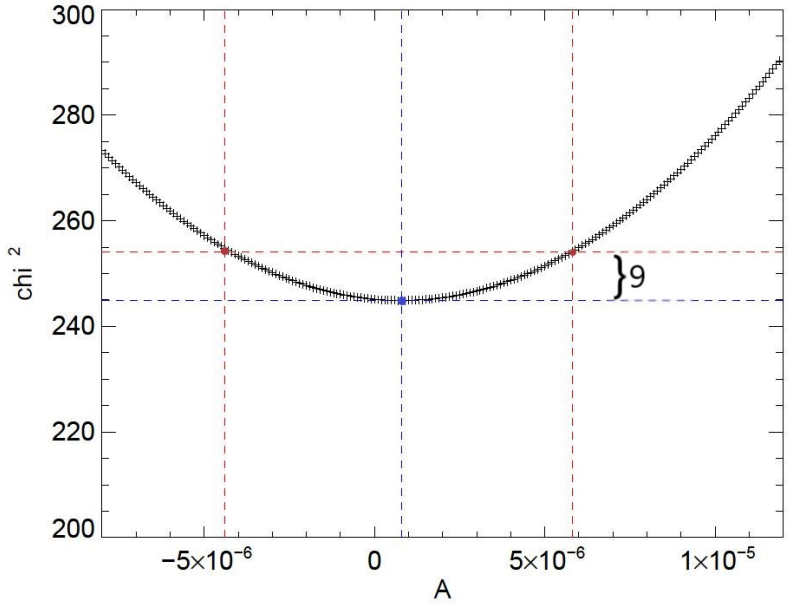

Figure 5.5: Illustration of the upper limit procedure with χ^2_{min} marked as blue dot and the 3σ upper and lower limits marked with red dots

Time [d]	Flux [10^{-4}ph cm^{-2}s^{-1}]	Center [keV]	Width [keV]
16.3 - 30.0	2.11	1282.4	21.6
30.0 - 50.0	2.18	1282.4	21.6
50.0 - 70.0	1.35	1319.0	16.8

Table 5.3: Parameters and upper limit fluxes of the ^{48}V line near 1312 keV in three different epochs

Also for the second energy range (1240 − 1380 keV) the Doppler broadened width and the Doppler shifted centroid energy were calculated with the bulk motion and velocity spread values from ^{56}Co analysis listed up in table 7.1. Again upper limits were set and the results are shown in figure 5.7. The parameter values are summed up in table 5.3.

For these upper limit fluxes of the three epochs the ejected mass of ^{48}V in each case is calculated with equation 18 and an atomic mass of $m_{^{48}V}$ = 47.95 u. For the 984 keV line the calculated mean mass is $M = 0.077$ M$_\odot$ and for the 1312 keV line it was determined to $M = 0.128$ M$_\odot$. Predictions of models are in the order of $\sim 10^{-4}$M$_\odot$ in delayed detonation models and up to 0.011 M$_\odot$ for a He detonation model which results from the explosion of a 1 $M_\odot$ white dwarf with a He envelope and an ejected ^{56}Ni mass of 0.56 M$_\odot$. The stated upper limit masses are too large to exclude specific models. [29] [28]

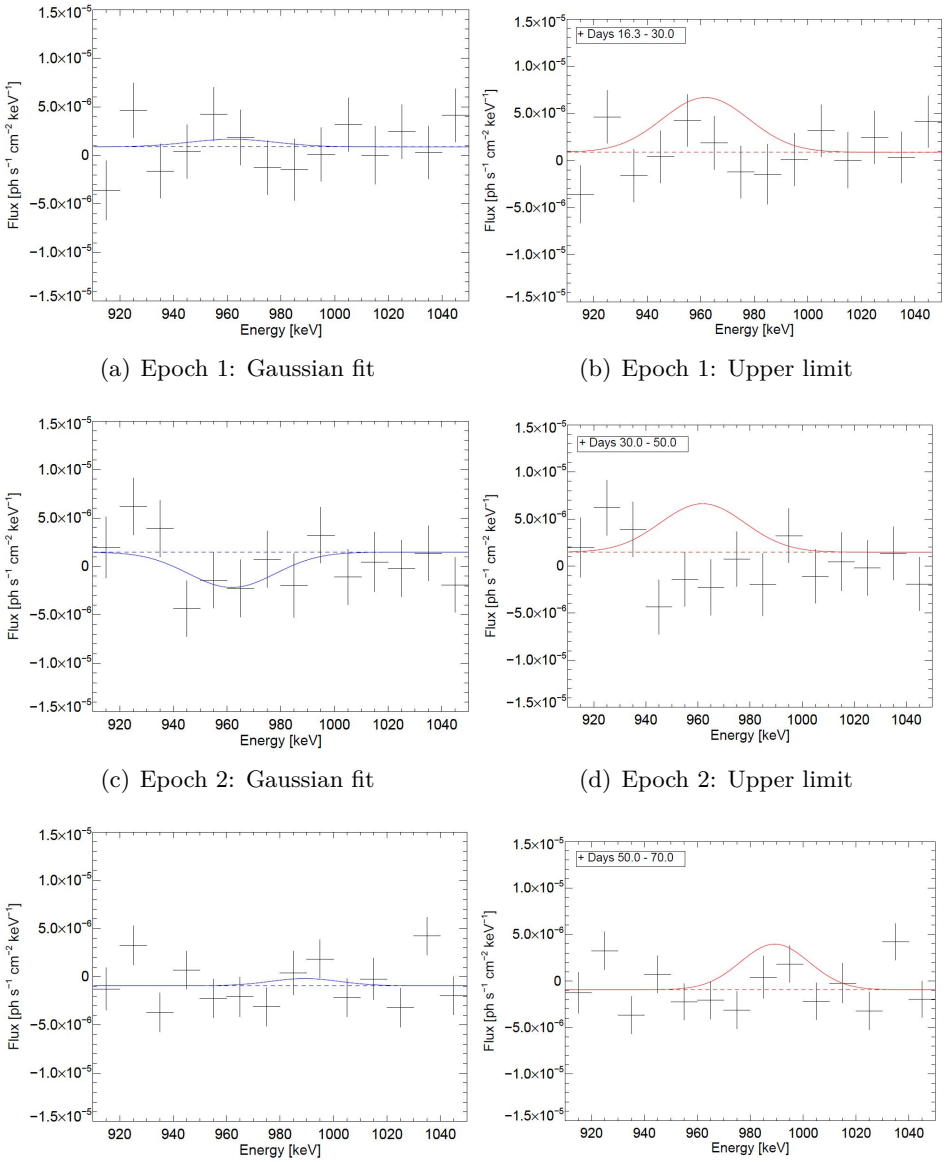

(a) Epoch 1: Gaussian fit

(b) Epoch 1: Upper limit

(c) Epoch 2: Gaussian fit

(d) Epoch 2: Upper limit

(e) Epoch 3: Gaussian fit

(f) Epoch 3: Upper limit

Figure 5.6: Spectra near the 984 keV line of ^{48}V in three epochs past explosion with Gaussian fits in blue and 3 σ signal upper limits plotted in red

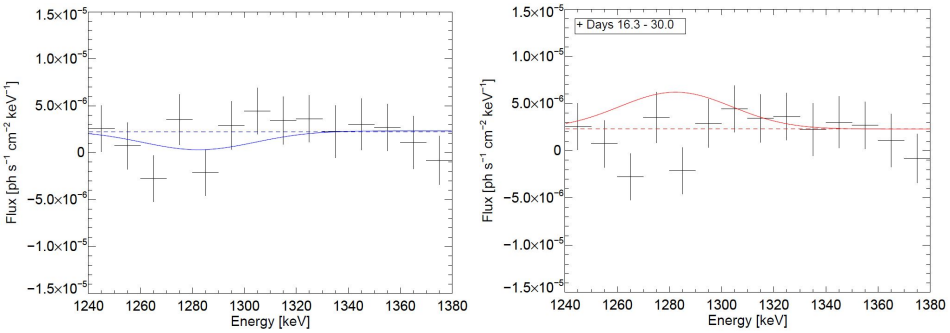

(a) Epoch 1: Gaussian fit

(b) Epoch 1: Upper limit

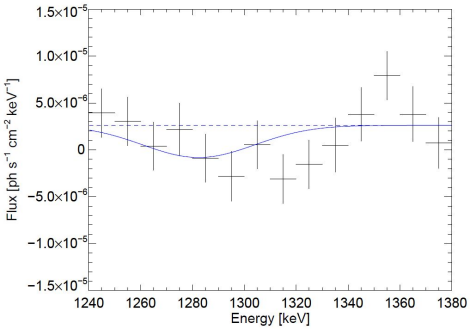

(c) Epoch 2: Gaussian fit

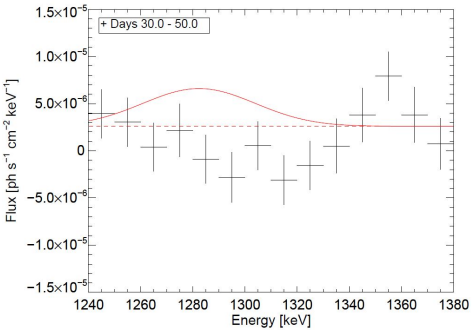

(d) Epoch 2: Upper limit

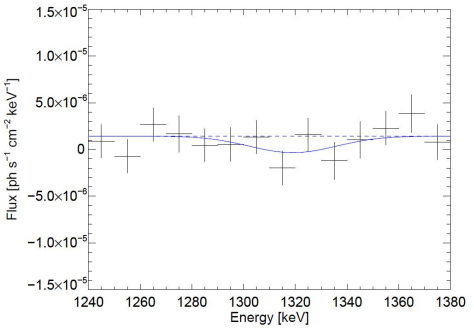

(e) Epoch 3: Gaussian fit

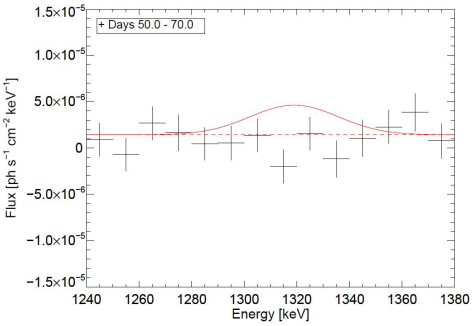

(f) Epoch 3: Upper limit

Figure 5.7: Spectra near the 1312 keV line of ^{48}V in three epochs past explosion with Gaussian fits in blue and 3 σ signal upper limits plotted in red

5.3 ^{57}Co

The third element that is searched for in the spectrum of the SN2014J is another radioactive iron group element: ^{57}Co. As delayed detonation models predict ^{57}Ni masses of the order $\sim 10^{-2}$M$_\odot$ and the decay product ^{57}Co has a lifetime of 392 days, it is a possible candidate for detection. [28] ^{57}Co decays via electron capture into the stable ^{57}Fe with a half-life of 271.79 d. During this decay a photon is released with an energy of 122.061 keV having 85.60% of the line intensity. [32]

As ^{57}Co has a long lifetime compared to the observation time, the spectrum is not time resolved as this would lead to a lower sensitivity. First a Gaussian shaped line is fitted with the model parameters A, σ and c. The centroid energy E_0 is fitted with parameter limits set to 117 keV and 127 keV so a Doppler shifted E_0, which can be shifted up to a value of $\Delta E = 2.8$ keV calculated with the highest velocity from the first epoch in table 7.1, is well within the limits. The χ^2 of that fit is $\chi^2 = 395.22$ with $\chi^2_{red} = 1.44$ and the best fit parameter values are $A = 5.28 \pm 1.67 \cdot 10^{-6}$ph cm^{-2}s^{-1}keV^{-1}, $\sigma = 7.89 \pm 1.57$ keV, $c = -1.37 \pm 5.14 \cdot 10^{-7}$ph cm^{-2}s^{-1}keV^{-1} and $E_0 = 118.73 \pm 2.20$ keV. The fit is checked against the null hypothesis that there is only the underlying continuum $c = 9.23 \pm 5.47 \cdot 10^{-7}$ph cm^{-2}s^{-1}keV^{-1} with $\chi^2 = 405.2$. The null hypothesis can be rejected by a significance of 3.16σ. The fit is shown in figure 5.8 with 10 keV energy bins.

The mass calculated with the resulting line flux of $1.04 \pm 0.39 10^{-4}$ph cm^{-2}s^{-1} has a value of $M = 0.32 \pm 0.12$ M$_\odot$. The mass predictions of delayed detonation models with a different number of ignition spots all are in the order of $\sim 10^{-2}$ M$_\odot$. [28] However, two strong background lines can be found in the raw spectrum in the energy range of the line shown in figure 5.9. It is possible that these lines are not efficiently suppressed and contribute to the high flux and significance of that line although the residuals in the energy range 100-135 calculated per 2.5 keV energy bins shown in figure 5.10 indicate a good fit, with Gaussian fit parameters of $\mu = -0.010 \pm 0.014$ and $\sigma = 1.002 \pm 0.015$. Furthermore, the high red shift indicates that the ^{57}Co is moving away from the detector with a speed of 8100 ± 5400 km s^{-1}. Compared to the bulk motion of ^{56}Co listed in table 7.1 the values are different. The large error bars of the fluxes at for example 55 keV, 65 keV and 95 keV prevent significant statements.

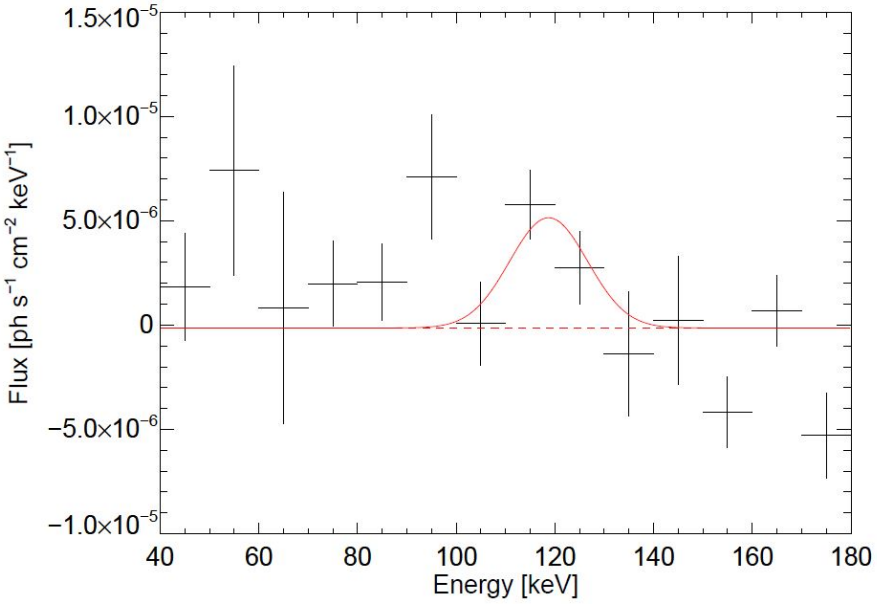

Figure 5.8: Gaussian fit of the 122 keV gamma-ray line of ^{57}Co with parameter limits for E_0

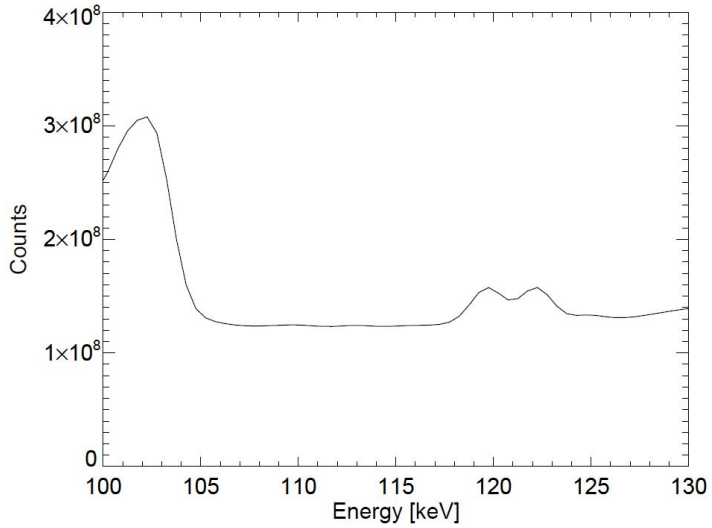

Figure 5.9: Spectrum of the measured counts from all detectors and all orbits in the energy range of 100 - 130 keV with two strong background lines near 120 keV

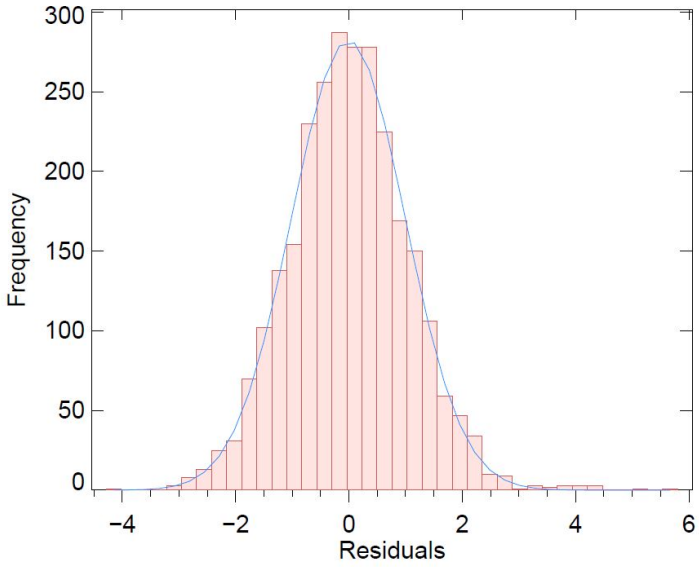

Figure 5.10: Histogram plot of the normalized residuals of the background model fit in the energy range 100-135 keV

6 Summary and outlook

The nearby SN2014J offers a great opportunity to gain more observational information about type Ia supernovae. This gamma-ray source was observed by the SPI detector on INTEGRAL over 112 days in total and thus, provides a good data set for further analysis. In order to distinguish between the large dominating instrumental background and the celestial gamma-rays originating from the source, a model is created to describe the data. The background description is derived from empirical approaches with information gained from long-term analysis and is composed of a variety of lines with an underlying continuum. Gamma-rays from radioative decays have well-defined energies apart from broadening, so peaks in the spectra near those energies can be analysed with Gaussian fits with constant offsets. With the high line sensitivity and fine energy resolution of the 19 germanium detectors of SPI, information about the flux and the kinematics of the decaying nuclide can be obtained. As the gamma-ray lines from the radioactive ^{56}Co have already been analysed in detail, other radioactive elements produced in type Ia supernovae were searched for. The selection is limited as the lifetime of many isotopes excludes possible detections in the observation time interval. Another selection criterion were mass predictions of the radioactive nuclides for different delayed detonation models (see [28]).
The elements were ^{48}V and ^{57}Co apart from ^{56}Co which meet most the requirements. The ^{56}Co line could be observed very well with a significance above 3σ and time resolved spectra provide intensity profiles. The derived velocity and speed values were used as a basis for the kinematics of other ejected elements. The reproduction of ^{56}Co results showed lower line fluxes and consequently also lower ^{56}Ni masses. For the two ^{48}V gamma-ray lines at 984 keV and 1312 keV only upper limits could be stated which give the maximum flux value that could be emitted by the source having still a certain probability of remaining undetected. The threshold is set to 3σ. With the mass values calculated with these upper limit fluxes no explosion model could be excluded. The analysis of the spectrum near the ^{57}Co 122 keV line showed a significant red shifted line with a mass of $M = 0.32 \pm 0.12$ M$_\odot$. Two strong background lines in the raw data from spacecraft material could contribute to the high flux in that energy range although the normalized residuals comparing the background model to the event counts do not show extreme outliers. Consequently, this value has to be viewed with precaution. Despite model fitting the impact of background noise makes it difficult to analyse celestial gamma-ray lines in the recorded spectra. This is especially true in ranges containing strong instrumental background lines from the germanium detectors themselves or surrounding material. However, the analysis of ^{56}Co shows that gamma-ray line spectroscopy helps to gain a lot of information about the elements produced and ejected by type Ia su-

pernovae if they are sufficiently nearby and nucleosynthetic yields are high enough.

References

[1] *Activity, Half-life and Decay constant*. Accessed: 25.07.18. URL: https://miniphysics.com/activity-half-life-and-decay-constant.html.

[2] Rene Andrae. *Error estimation in astronomy: A guide*. Accessed: 23.07.18. 2010. eprint: arXiv:1009.2755. URL: http://inspirehep.net/record/868729/plots.

[3] *Berechnung der Fläche unter der Gausskurve*. Accessed: 24.07.18. URL: http://wwwex.physik.uni-ulm.de/lehre/gk2-2007/node55.html.

[4] *Big Bang Nucleosynthesis*. Accessed: 24.07.18. URL: http://astro.ucla.edu/~wright/BBNS.html.

[5] *Blackbody Radiation*. Accessed: 02.08.18. URL: http://astronomy.swin.edu.au/cosmos/B/Blackbody+Radiation.

[6] Samprit Chatterjee. "Residuals". In: *International Encyclopedia of Statistical Science*. Ed. by Miodrag Lovric. Berlin, Heidelberg: Springer Berlin Heidelberg, 2011, pp. 1227–1229. ISBN: 978-3-642-04898-2. DOI: 10.1007/978-3-642-04898-2_491. URL: https://doi.org/10.1007/978-3-642-04898-2_491.

[7] R. Diehl, D. H. Hartmann, and N. Prantzos, eds. *Astrophysics with Radioactivities, An Introduction to Astrophysics with Decaying Isotopes*. Springer Verlag, 2018.

[8] Roland Diehl. "Nuclear-Astrophysics Lessons from INTEGRAL". In: *Reports on Progress in Physics* vol. 76.2 (2013). DOI: 10.1088/0034-4885/76/2/026301. eprint: arXiv:1302.3441.

[9] Roland Diehl et al. "INTEGRAL/SPI γ-ray line spectroscopy". In: *Astronomy and Astrophysics* (2017). DOI: 10.1051/0004-6361/201731815. eprint: arXiv:1710.10139.

[10] Roland Diehl et al. "SN2014J gamma-rays from the 56Ni decay chain". In: *Astronomy and Astrophysics* (2014). DOI: 10.1051/0004-6361/201424991. eprint: arXiv:1409.5477.

[11] T. Hebbeker. *Statistik - Fehlerrechnung - Auswertung von Messungen*. Accessed: 23.07.18. URL: https://web.physik.rwth-aachen.de/~hebbeker/lectures/stat_fprakt_1.pdf.

[12] Matthias Heyssler. *Das Leben der Sterne, Teil II: Junge stellare Objekte und Sternenalltag*. Springer Spektrum, Wiesbaden, 2015. DOI: 10.1007/978-3-658-09173-6. URL: https://doi.org/10.1007/978-3-658-09173-6.

[13] Matthias Heyssler. *Das Leben der Sterne, Teil III: Endphasen der Sterne*. Springer Spektrum, Wiesbaden, 2016. DOI: 10.1007/978-3-658-10650-8. URL: https://doi.org/10.1007/978-3-658-10650-8.

[14] W. Hillebrandt et al. "Towards an understanding of Type Ia supernovae from a synthesis of theory and observations". In: *Frontiers of Physics* (2013). DOI: 10.1007/s11467-013-0303-2. eprint: arXiv:1302.6420.

[15] *Interaction of Gamma Radiation with Matter*. Accessed: 02.08.18. URL: https://nuclear-power.net/nuclear-power/reactor-physics/interaction-radiation-matter/interaction-gamma-radiation-matter/.

[16] Vinay L. Kashyap et al. *What is an Upper Limit?* 2008. URL: https://hea-www.harvard.edu/AstroStat/HEAD2008/poster_vkashyap.pdf.

[17] Glenn E Knoll. *Radiation Detection And Measurement, 3rd Edition*. Wiley India, 2009. ISBN: 8126522607. URL: https://amazon.com/Radiation-Detection-Measurement-3rd-Ed/dp/8126522607.

[18] William R. Leo. *Techniques for Nuclear and Particle Physics Experiments*. Springer-Verlag Berlin Heidelberg, 1994, pp. 215–247. DOI: 10.1007/978-3-642-57920-2. URL: https://doi.org/10.1007/978-3-642-57920-2.

[19] *Linewidths*. Accessed: 23.07.18. URL: http://www-star.st-and.ac.uk/~kw25/teaching/nebulae/lecture08_linewidths.pdf.

[20] D. K. Nadyozhin. "The properties of NI to CO to Fe decay". In: *The Astrophysical Journal Supplement Series* 92 (1994), pp. 527–531. DOI: 10.1086/192008. URL: http://adsabs.harvard.edu/abs/1994ApJS...92..527N.

[21] Ken'ichi Nomoto and Shing-Chi Leung. "Single Degenerate Models for Type Ia Supernovae Progenitor's Evolution and Nucleosythesis Yields". In: *Space Science Reviews* vol. 214 (2018). DOI: 10.1007/s11214-018-0499-0. eprint: arXiv:1805.10811.

[22] R. Pakmor et al. “Normal type Ia supernovae from violent mergers of white dwarf binaries”. In: *The Astrophysical Journal Letters* vol. 747.1 (2012). DOI: 10.1088/2041-8205/747/1/L10. URL: http://stacks.iop.org/2041-8205/747/i=1/a=L10.

[23] William H. Press et al. *Numerical Recipes in Fortran 77, The Art of Scientific Computing, Second Edition*. Cambridge University Press, 1992. ISBN: 052143064X.

[24] *Radiation Pressure*. Accessed: 01.08.2018. URL: http://astronomy.swin.edu.au/cosmos/R/radiation+pressure.

[25] *Roche-lobe*. Accessed: 02.07.18. URL: http://astronomy.swin.edu.au/cosmos/R/Roche-lobe.

[26] F. K. Roepke. “Thermonuclear Supernovae”. In: *Proceedings of Science* (2008). eprint: arXiv:0804.2147.

[27] Ivo R. Seitenzahl and Dean M. Townsley. “Nucleosynthesis in thermonuclear supernovae”. In: (2017). DOI: 10.1007/978-3-319-21846-5_87. eprint: arXiv:1704.00415.

[28] Ivo R. Seitenzahl et al. “Three-dimensional delayed-detonation models with nucleosynthesis for Type Ia supernovae”. In: *Monthly Notices of the Royal Astronomical Society* 429.2 (2013), pp. 1156–1172. DOI: 10.1093/mnras/sts402. eprint: /oup/backfile/content_public/journal/mnras/429/2/10.1093_mnras_sts402/1/sts402.pdf. URL: http://dx.doi.org/10.1093/mnras/sts402.

[29] Ken J. Shen et al. “Thermonuclear .Ia Supernovae from Helium Shell Detonations: Explosion Models and Observables”. In: *The Astrophysical Journal* 715.2 (2010), p. 767. URL: http://stacks.iop.org/0004-637X/715/i=2/a=767.

[30] *Table of Radioactive Isotopes,* ^{48}V. Accessed: 24.07.18. URL: http://nucleardata.nuclear.lu.se/toi/nuclide.asp?iZA=230048.

[31] *Table of Radioactive Isotopes,* ^{56}Co. Accessed: 24.07.18. URL: http://nucleardata.nuclear.lu.se/toi/nuclide.asp?iZA=270056.

[32] *Table of Radioactive Isotopes,* ^{57}Co. Accessed: 24.07.18. URL: http://nucleardata.nuclear.lu.se/toi/nuclide.asp?iZA=270057.

[33] *The Doppler Effect*. Accessed: 23.07.18. URL: https://courses.lumenlearning.com/astronomy/chapter/the-doppler-effect/.

[34] *Things that go Bang in the Night*. Accessed: 24.07.18. URL: http://community.dur.ac.uk/john.lucey/bridge/SN2014J_bridge.html.

[35] Vedrenne, G. et al. "SPI: The spectrometer aboard INTEGRAL". In: *A&A* 411.1 (2003), pp. L63–L70. DOI: 10.1051/0004-6361:20031482. URL: https://doi.org/10.1051/0004-6361:20031482.

[36] Winkler, C. et al. "The INTEGRAL mission". In: *A&A* 411.1 (2003), pp. L1–L6. DOI: 10.1051/0004-6361:20031288. URL: https://doi.org/10.1051/0004-6361:20031288.

[37] S. E. Woosley and Daniel Kasen. "Sub-Chandrasekhar Mass Models For Type Ia Supernovae". In: (2010). DOI: 10.1088/0004-637X/734/1/38. eprint: arXiv:1010.5292.

List of Figures

List of Tables

7 Appendix

Time [d]	Bulk [km s^{-1}]	Spread [km s^{-1}]
16.3 - 41.3	-6920 ± 1480	5060 ± 1330
41.3 - 66.3	1600 ± 1720	3940 ± 1260
66.3 - 99.1	1600 ± 1600	7250 ± 1560
134.8 - 164.0	-80 ± 1870	4570 ± 1840

Table 7.1: Velocity values adapted from [10] for the whole observation time split into four epochs